Quantitative Monte Carlo–Based ^{90}Y SPECT Reconstruction

Mattijs Elschot[1], Marnix G.E.H. Lam[1], Maurice A.A.J. van den Bosch[1], Max A. Viergever[2], and Hugo W.A.M. de Jong[1]

[1]*Department of Radiology and Nuclear Medicine, University Medical Center Utrecht, Utrecht, The Netherlands; and* [2]*Image Sciences Institute, University Medical Center Utrecht, Utrecht, The Netherlands*

The evaluation of radiation absorbed doses in tumorous and healthy tissues is of increasing interest for ^{90}Y microsphere radioembolization of liver malignancies. The objectives of this work were to introduce and validate a new reconstruction method for quantitative ^{90}Y bremsstrahlung SPECT to improve posttreatment dosimetry. **Methods:** A fast Monte Carlo simulator was adapted for ^{90}Y and incorporated into a statistical reconstruction algorithm (SPECT-MC). Photon scatter and attenuation for all photons sampled from the full ^{90}Y energy spectrum were modeled during reconstruction by Monte Carlo simulations. The energy- and distance-dependent collimator–detector response was modeled with precalculated convolution kernels. The National Electrical Manufacturers Association 2007/International Electrotechnical Commission 2008 image quality phantom was used to quantitatively evaluate the performance of SPECT-MC in comparison with those of state-of-the-art clinical SPECT reconstruction and PET. The liver radiation absorbed doses estimated by SPECT, PET, and SPECT-MC were evaluated in 5 patients consecutively treated with radioembolization. **Results:** In comparison with state-of-the-art clinical ^{90}Y SPECT reconstruction, SPECT-MC substantially improved image contrast (e.g., from 25% to 88% for the 37-mm sphere) and decreased the mean residual count error in the lung insert (from 73% to 15%) at the cost of higher image noise. Image noise and the mean count error were lower for SPECT-MC than for PET. Image contrast was higher in the larger spheres (diameter of ≥28 mm) but lower in the smaller spheres (≤22 mm) for SPECT-MC than for PET. In the clinical study, mean absorbed dose estimates in liver regions with high absorbed doses were consistently higher for SPECT-MC than for SPECT ($P = 0.0625$) and consistently higher for SPECT-MC than for PET ($P = 0.0625$). **Conclusion:** The quantitative accuracy of ^{90}Y bremsstrahlung SPECT is substantially improved by Monte Carlo–based modeling of the image-degrading factors. Consequently, ^{90}Y bremsstrahlung SPECT may be used as an alternative to ^{90}Y PET.

Key Words: radioembolization; ^{90}Y; SPECT/CT; reconstruction; dosimetry

J Nucl Med 2013; 54:1557–1563
DOI: 10.2967/jnumed.112.119131

The high-energy β-emitter ^{90}Y is used in clinical practice for several radiotherapeutic applications, including intraarterial microsphere radioembolization for the treatment of nonresectable liver tumors (*1,2*). For enabling the evaluation of radiation absorbed doses in tumorous and healthy liver tissues, posttreatment imaging of the ^{90}Y microsphere distribution has recently gained interest (*3–5*).

Assessment of the ^{90}Y microsphere distribution can be performed by imaging bremsstrahlung photons with a SPECT camera or by imaging annihilation photons with a PET camera. Posttreatment dosimetry with ^{90}Y PET has advantages over SPECT, mainly because of higher resolution and image contrast (*6,7*). However, the low positron branch (32×10^{-6}) in ^{90}Y decay requires a state-of-the-art lutetium-(yttrium)-orthosilicate time-of-flight PET/CT scanner to obtain images with sufficiently high quantitative accuracy for dosimetry purposes (*8,9*). Posttreatment imaging with a standard SPECT/CT system may be a more widely available and cost-effective option for most centers, but the image quality (IQ) of state-of-the-art clinical ^{90}Y bremsstrahlung SPECT is still limited (*7*). The wide range (0–2.3 MeV) and continuous nature of the ^{90}Y bremsstrahlung photon spectrum prohibit the use of simple energy window–based scatter rejection and correction techniques, hinder attenuation correction based on single-photon energy, and require compensation for collimator- and detector-related image-degrading effects, such as collimator scatter, lead x-rays, septal penetration, camera (back)scatter, and partial energy deposition in the crystal (*10*). The shape and magnitude of these effects depend on photon energy, tissue composition, collimator and detector characteristics, the distance between the source and the collimator, and the energy window settings.

To date, clinically available reconstruction algorithms have not been able to adequately compensate for the image-degrading effects that limit quantitative ^{90}Y bremsstrahlung SPECT. However, it was recently shown by Rong et al. that extensive modeling of scatter and attenuation effects and the collimator–detector response (CDR) improved activity quantification for ^{90}Y SPECT (*11*). In their approach, Monte Carlo simulations were used to precalculate energy-dependent scatter kernels and energy- and distance-dependent CDR tables, which were subsequently applied during reconstruction. In this study, we propose a new model-based ^{90}Y SPECT reconstruction algorithm that makes use of a fast Monte Carlo simulator for "on-the-fly" calculation of the scatter and attenuation effects in patients instead of precalculated scatter kernels. These Monte Carlo simulations are performed anew for every patient, during every update of the reconstruction process. The hypothetical advantage of this approach is that all photon transport physics can be included in a detailed and accurate way, irrespective of source distribution, photon energy, scatter order, nonuniform tissue density, and other complicating factors (*12,13*). Only the photon interactions in the collimator are modeled with precalculated kernels.

The quantitative accuracy of the proposed reconstruction method is evaluated and compared with those of state-of-the-art clinically available ^{90}Y bremsstrahlung SPECT and ^{90}Y PET in

Received Dec. 26, 2012; revision accepted Apr. 23, 2013.
For correspondence or reprints contact: Mattijs Elschot, P.O. Box 85500, Room E01.132, 3508 GA Utrecht, The Netherlands.
E-mail: m.elschot@umcutrecht.nl
Published online Aug. 8, 2013.

phantom experiments. Additionally, intrahepatic dosimetry is performed and evaluated in 5 patients treated with ^{90}Y radioembolization in clinical practice.

MATERIALS AND METHODS

The Utrecht Monte Carlo System (UMCS) is a validated, fully 3-dimensional (3D) Monte Carlo–based approach for the simulation of γ-camera projection images of a radionuclide distribution. UMCS is fast enough for on-the-fly photon transport calculation in a statistical image reconstruction algorithm. An extensive description of standard UMCS has been given elsewhere (*13,14*). The approach has been validated for the simulation of ^{99m}Tc (*15*) and ^{201}Tl projections (*16*). In contrast to ^{90}Y, however, these radionuclides do not require the simulation of high-energy photon contributions to a lower-energy detection window. For the purpose of this work, UMCS was adapted to simulate ^{90}Y projection images, including photon contributions from the full ^{90}Y energy spectrum.

UMCS Physics

Two major adaptations to standard UMCS (*14*) were made so that the approach would be suitable for the simulation of ^{90}Y projection images: the source photon energies were sampled from a continuous energy spectrum, and the energy dependency of the CDR was modeled, including all collimator- and detector-related image-degrading effects. Schematic overviews of UMCS physics are shown in Figure 1.

Source Photon Energy Sampling. We implemented the ^{90}Y photon energy spectrum as a combination of the ^{90}Y bremsstrahlung spectrum, generated with MCNPX, version 2.5.0 (*17*); the 511-keV annihilation photon peak (3.2×10^{-5} cps Bq^{-1}); and the 1,760-keV prompt γ-peak (7.8×10^{-5} cps Bq^{-1}) (*18,19*). β-particle physics were not implemented in UMCS. Photon emission energies were directly sampled from the ^{90}Y photon energy distribution, and photons were emitted from the point of decay. In reality, bremsstrahlung photons are created along the tract of the β-particle, introducing additional blurring. This effect was included in the CDR (see "Precalculation of CDR Kernels" later in the article). After photon emission, standard UMCS scatter and attenuation models were used for the calculation of photon transport in patients.

Simulation of Scatter Maps. In this study, photons were first traced from their emission position to their final scatter position via up to 10 scatter events. For each scatter event, the photon intensity (i.e., probability of existence), position, direction, and energy were recorded. Subsequently, for every camera angle, photons were forced to Compton scatter (coherent scatter was not included) from each recorded scatter position toward the detector, and the photon intensities were updated accordingly (Fig. 1A). For the purpose of computationally efficient modeling of the distance- and energy-dependent CDR, the updated photon intensities were binned voxelwise in 8 energy-dependent, 3D scatter maps according to their energy after the last scatter event (i.e., toward the detector). The energy limits of the scatter maps are shown in Figure 1B.

Photon Detection. Photons of all energies may contribute to the detection window (in this study, 50–250 keV), for example, through collimator scatter, lead x-rays, or partial energy deposition in the crystal (*10*). These effects are modeled by the CDR in the photon detection model. To simulate energy-dependent photon detection, we made use of techniques that have been developed for the fast simulation of downscatter projections for dual-isotope SPECT (*20*). The detection process was performed separately for each of the 8 scatter maps, in 2 steps.

First, for each voxel of the scatter map, the photon attenuation in the patient on the path toward the detector was approximated with a scatter map–specific attenuation coefficient ($\mu_{central}$) (Fig. 1B), which was the central μ-value of the energy range of the scatter map (bin). Second, the attenuation-corrected scatter maps were blurred layer by layer by convolution with the precalculated distance-dependent CDRs, which represented the spatially varying detection probability of the corresponding photon energy ($E_{\mu\text{-central}}$) (Fig. 1B) if measured in air at a given distance from the collimator (see "Precalculation of CDR Kernels" later in the

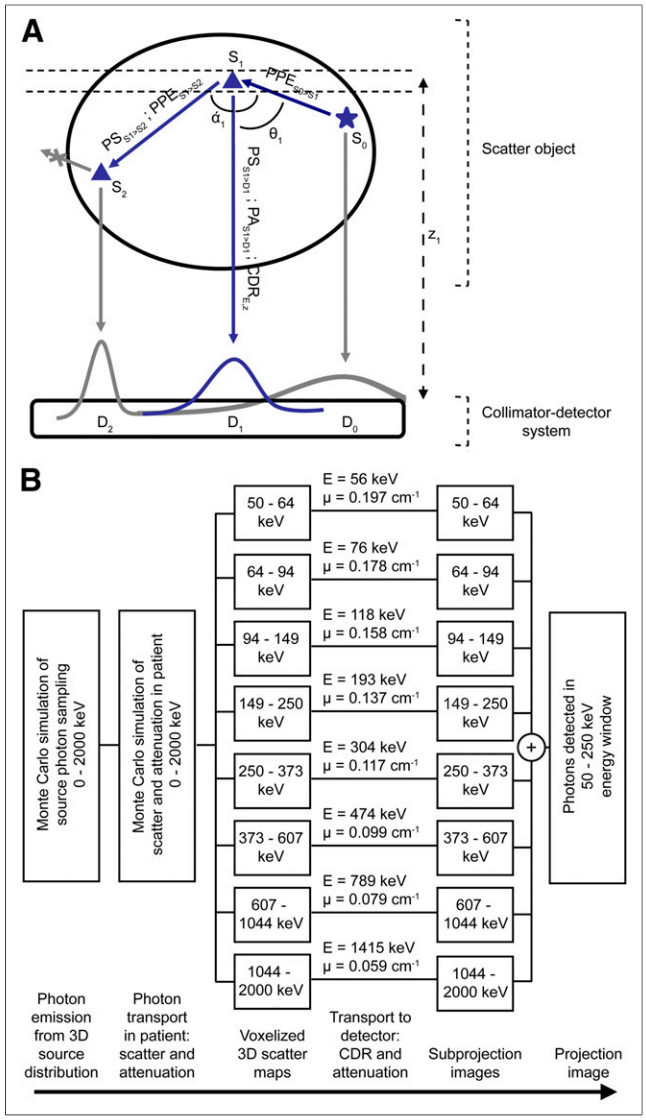

FIGURE 1. Schematic overview of UMCS physics models in scatter object and collimator–detector system (A) and of subsequent steps involved in simulation of 2-dimensional projection images from 3D source distribution (B). After photon emission (S_0), probability of existence of photon at scatter position S_n ($1 \leq n \leq 10$) is dependent on probability of not having been absorbed photoelectrically (PPE) and on probability of scattering over angle α_n [PS(α_n)]. From each position S_n ($0 \leq n \leq 10$), copy of photon is forced to scatter over angle θ_n toward detector. Photon detection probability at position D_n depends on probability of scatter over angle θ_n [PS(θ_n)], on probability of not having been attenuated by scatter object (PA), and on shape and magnitude of distance (z_n)- and energy-dependent CDR. In last 2 steps (i.e., PA and CDR), which are performed after voxelwise binning of photon intensities in energy-dependent 3D scatter maps, attenuation coefficient is approximated by $\mu_{central}$ (μ in B) and CDR is approximated by CDR of $E_{\mu\text{-central}}$ (E in B).

article). Subsequently, the blurred, attenuation-corrected scatter maps were summed over the direction perpendicular to the camera face to form 2-dimensional subprojection images. The sum of all energy-dependent subprojection images formed the final simulated projection image for the given camera angle.

Precalculation of CDR Kernels. An MCNPX model of the camera head of a Siemens Symbia T16 SPECT/CT system with a mounted high-energy collimator was developed to precalculate distance-dependent CDRs. For each of the 8 scatter maps, photons with $E_{\mu\text{-central}}$ were emitted in air and detected in an energy window of 50–250 keV. To take into account the creation of bremsstrahlung photons along the tract of the β-particle, we sampled photon emission positions uniformly from a sphere (containing air) with a radius of 3.15 mm. This approach resulted in a mean radial photon emission position of 2.5 mm, which corresponded to the mean range of the β-particles in tissue. The CDRs were radially averaged after detection to reduce the required calculation time.

Validation of UMCS. Before application in SPECT reconstruction, the accuracy of the UMCS-simulated projection images was evaluated in 2 γ-camera experiments. The number of simulated photons was 10^6. Measurements were performed with a dual-head Siemens Symbia T16 SPECT/CT system with mounted high-energy collimators. Photons were detected in an energy window of 50–250 keV on a 128 × 128 matrix with a pixel size of 4.8 × 4.8 mm^2.

In the first experiment, a 1-mm-diameter line source was centered in a polymethyl methacrylate scatter object measuring 40 × 40 × 20 cm^3. Line spread functions, summed over 10-cm-wide profiles and normalized to their maximum value, were compared visually and by means of the area under the curve between the measurement and the UMCS simulation. The measured line spread function was also compared with an MCNPX simulation (10^9 photons) to validate the camera geometry for calculation of the CDRs. In the second experiment, the National Electrical Manufacturers Association 2007/International Electrotechnical Commission 2008 PET IQ phantom was filled with ^{90}Y activity concentrations of 0.27 MBq mL^{-1} in the torso-shaped compartment and 2.40 MBq mL^{-1} in the 6 fillable coplanar spheres (inner diameters of 10, 13, 17, 22, 28, and 37 mm) and with no activity in the cylindric lung insert (outer diameter of 51 mm). Ten-centimeter-wide profiles through the measured and UMCS-simulated projection images were compared.

^{90}Y Bremsstrahlung SPECT Reconstruction

UMCS was incorporated in a dual-matrix ordered-subsets expectation maximization reconstruction framework (*21*) for Monte Carlo–based ^{90}Y SPECT reconstruction. In dual-matrix ordered-subsets expectation maximization, the forward projector is not identical to the back projector; that is, more approximate photon transport models are used in the backprojection step. This approach accelerates reconstruction but has minimal impact on IQ (*13,21,22*). In the forward projector, nonuniform photon attenuation, photon scatter, and the distance- and energy-dependent CDR were modeled as explained earlier. The number of simulated photons per projection was 10^6. In the backprojection step, photon attenuation was approximated with a single μ-value (instead of 8 μ-values) corresponding to the central energy of the acquisition window, photon scatter was not modeled, and the CDR was modeled with a distance-dependent gaussian function. We refer to the proposed SPECT reconstruction method as SPECT-MC in the remainder of this work.

IQ Phantom Experiment. The accuracy of SPECT-MC in comparison with those of state-of-the-art clinical SPECT and PET was quantitatively evaluated by use of the IQ phantom with the activity distribution described earlier (see "Validation of UMCS").

SPECT data were acquired by use of the Siemens Symbia T16 SPECT/CT system with 120 angles over a 360° orbit and an energy window of 50–250 keV. The acquisition time was 120 s/projection (120 min in total), resulting in a count density similar to that of a 30-min-long acquisition of a clinically realistic liver activity concentration of approximately 1 MBq mL^{-1}. SPECT-MC data were reconstructed to a voxel size of 4.8 × 4.8 × 4.8 mm^3 by use of 60 iterations with 8 subsets. No postreconstruction filter was applied. State-of-the-art clinical SPECT reconstruction was performed with Siemens FLASH3D (8 iterations, 8 subsets, no postreconstruction filter). Attenuation correction was performed with an effective broad-beam linear attenuation coefficient of 0.034 cm^{-1}. Scatter correction was not included. PET data were acquired with a Siemens mCT time-of-flight PET/CT scanner in 1 bed position centered on the spheres. The total acquisition time was half the SPECT acquisition time (60 min) because the PET field of view covering a whole liver generally requires 2 bed positions. PET images were reconstructed with the standard clinical 3D iterative attenuation-weighted ordinary Poisson ordered-subsets expectation maximization algorithm (3 iterations, 21 subsets, 5-mm full width at half maximum postreconstruction filter), including resolution recovery and time-of-flight information, and correction for scattered and random events. The reconstructed voxel size was 2 × 2 × 2 mm^3.

Image contrast, noise, and the residual error after attenuation and scatter correction were compared among SPECT, PET, and SPECT-MC. In the slice through the center of the coplanar spheres, 6 circular regions of interest (ROIs) (diameters of 10, 13, 17, 22, 28, and 37 mm) were centered on the hot spheres, and a circular ROI (diameter of 30 mm) was centered on the lung insert. A background ROI defined in the same slice consisted of all voxels within the phantom except the hot-sphere ROI dilated by 10 mm and the physical lung insert. For each of the 6 hot-sphere ROIs, contrast recovery coefficients (Q_H) were calculated with the following equation:

$$Q_H = \frac{C_H/C_B - 1}{R - 1} \times 100\%, \qquad \text{Eq. 1}$$

Here, C_H is the mean intensity in the hot-sphere ROI, C_B is the mean intensity in the background ROI, and R is the sphere-to-background activity concentration ratio. The residual count error in the lung insert (ΔC_{lung}) was calculated with the following equation:

$$\Delta C_{lung} = \frac{C_{lung}}{C_B} \times 100\%, \qquad \text{Eq. 2}$$

Here, C_{lung} is the mean intensity in the lung insert ROI. As a measure of image noise, the coefficient of variation (CV) was calculated as follows:

$$CV = \frac{STDV_B}{C_B} \times 100\%, \qquad \text{Eq. 3}$$

Here, $STDV_B$ is the standard deviation over all voxels in the background ROI.

Patient Dosimetry. For clinical illustration, a comparison of SPECT-MC, SPECT, and PET was performed in 5 patients who underwent dual posttreatment imaging with SPECT/CT and PET/CT. This clinical study included a retrospective analysis of data gathered as part of the quality control protocol for the implementation of ^{90}Y PET as the standard postradioembolization imaging procedure. The Institutional Review Board of the University Medical Center Utrecht approved this retrospective study and waived the requirements for patient informed consent.

Radioembolization with ^{90}Y-labeled resin microspheres (SIR-Spheres; Sirtex) was successfully performed in 5 consecutive patients

TABLE 1
Patient and Treatment Characteristics

Patient	Primary disease*	Lobes treated†	Volume of treated liver (mL)	% of liver involved by tumor	A_A (MBq)	A_S (MBq)	A_P (MBq)
1	CRC	W	2,481	6	1,714	1,303	1,602
2	CRC	W	1,835	3	1,852	1,483	1,499
3	NPC	W	1,230	6	1,199	922	1,109
4	MC	L	383	5	281	216	270
5	HCC	W	3,050	6	1,177	916	927

*CRC = colorectal carcinoma; NPC = nasopharyngeal carcinoma; MC = mammary carcinoma; HCC = hepatocellular carcinoma.
†W = whole liver; L = left lobe.
A_A = activity administered to patient; A_S = activity at time of SPECT; A_P = activity at time of PET.

(2 women and 3 men; median age, 57 y; age range, 43–76 y) according to international consensus standards (*23*). The body surface area method (*23*) was used to calculate the activities. All patient and treatment characteristics are summarized in Table 1.

The total scan time was 30 min for both SPECT and PET, the latter requiring 2 bed positions centered on the liver. Images were reconstructed with the settings described earlier. Possible accumulation of activity in organs other than the liver was evaluated on posttreatment images. Liver ROIs were manually delineated on CT images, and 1-cm margins were automatically added to liver ROIs. The SPECT, PET, and SPECT-MC reconstructed counts were converted into units of activity by normalization of the total counts in the liver ROIs with 1-cm margins to the activities administered to the patients. For each patient, 1 integrated SPECT/PET/SPECT-MC high-absorbed-dose (HAD) ROI was defined and applied to all reconstructed images. This ROI consisted of all voxels with an activity concentration of at least 2 times the mean whole liver concentration on (at least) 1 of the 3 images to prevent bias toward any of the methods. Subsequently, low-absorbed-dose (LAD) ROIs were defined as the liver ROIs excluding the integrated HAD ROI. Absorbed dose images were created by convolution of the activity images with the appropriate ^{90}Y 3D dose–point kernel simulated with MCNPX, in accordance with MIRD Pamphlet No. 17 (*24*). Mean absorbed doses, standard deviations, and cumulative dose–volume histograms for the LAD and HAD ROIs were determined.

The same analysis was performed on a subvolume (~2.5 L) of the phantom including the hot spheres to enable comparison of the SPECT–, PET–, and SPECT-MC–estimated radiation absorbed doses in the integrated LAD and HAD ROIs with the known absorbed dose in the phantom (i.e., the gold standard). The trend observed in the performance of the 3 methods in the clinical study was compared with the trend observed in the phantom data.

Statistical Analysis

Descriptive parameters are presented as means and standard deviations and as medians and ranges. Statistical differences in contrast recovery coefficients and mean absorbed doses between reconstruction methods were analyzed with the nonparametric Wilcoxon signed rank test for paired data because normality could not be assumed with the small sample sizes. All tests were performed with a significance level of 0.05.

RESULTS

Validation of UMCS

The profiles through the simulated and measured projection images are shown in Figure 2. Good agreement between the UMCS and the measured projections was found in both the line source and the IQ phantom, although the tails of the UMCS profiles were slightly overestimated. The areas under the curve of the UMCS simulations were 5.7% and 1.3% higher than the areas under the curve of the measurements for the line source and the IQ phantom, respectively. The area under the curve of the MCNPX profile was overestimated by less than 1% in comparison with the measured line spread function. This excellent agreement validated the camera geometry used in MCNPX.

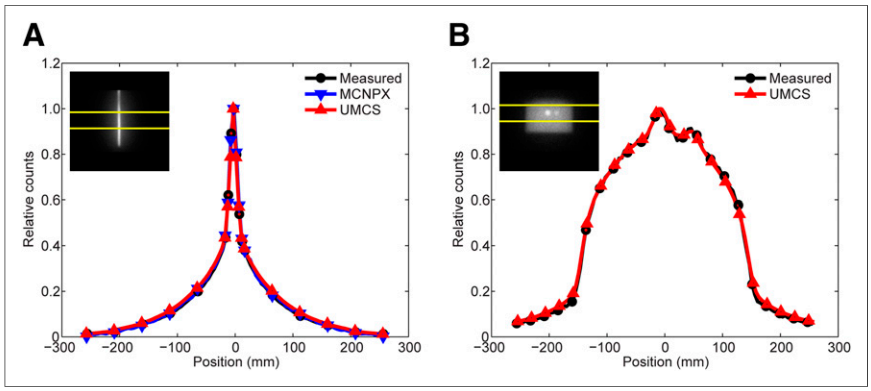

FIGURE 2. Profiles through measured and simulated projection images of line source centered in 20-cm scatter material (A) and IQ phantom (B). Profiles were summed over bins between yellow lines and normalized to their maximum value.

^{90}Y Bremsstrahlung SPECT Reconstruction

IQ Phantom Experiment. Image contrast, the residual count error in the lung insert, and image noise for the 3 methods are shown in Figure 3. Over all spheres, the SPECT-MC image contrast was significantly higher than the SPECT image contrast (P = 0.0313). Compared with the PET image contrast, the SPECT-MC image contrast was higher in the 2 largest spheres and lower in the 4 smallest spheres. Over all spheres, image contrast did not differ significantly (P = 0.3125) between PET and SPECT-MC. Image noise values were 14%, 47%, and 43% for SPECT, PET, and SPECT-MC, respectively. The residual

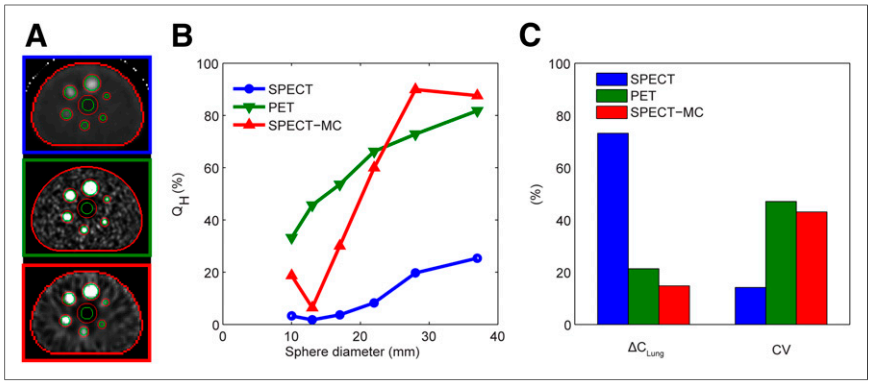

FIGURE 3. (A) Center slices through SPECT (blue), PET (green), and SPECT-MC (red) reconstructed images, overlaid with boundaries of hot-sphere and lung insert ROIs (green) and background ROI (red). All images were linearly window leveled from 0 to 6 times mean background intensity. (B) Hot-sphere contrast (Q_H) plotted as function of sphere diameter. (C) Residual count error in lung insert (ΔC_{lung}) and image noise (CV).

error in the lung ROI was lowest for SPECT-MC: 15% versus 73% and 21% for SPECT and PET, respectively.

Patient Dosimetry. No accumulation of activity outside the liver was found in any of the patients. Figure 4 shows an example of the SPECT–, PET–, and SPECT-MC–estimated activity concentration distributions in a patient. In comparison with the PET image, the SPECT-MC image had a lower resolution but was less affected by noise, in line with the results of the phantom study. However, in general, good correspondence between PET and SPECT-MC activity distributions was found. Compared with the PET and SPECT-MC distributions, the SPECT distribution had a reduced peak activity concentration and higher background activity concentrations in the tails.

Figure 5 shows that the estimated mean absorbed doses in the LAD ROIs were consistently (i.e., for each patient) lower with SPECT-MC than with PET (median difference, −1.4 Gy; range, −1.9 to −0.2 Gy; $P = 0.0625$) but not SPECT (median difference, 2.9 Gy; range, −1.9 to 3.8 Gy; $P = 0.1250$). The mean absorbed doses in the HAD ROIs were consistently higher with SPECT-MC than with SPECT (median difference, 33.9 Gy; range, 21.7–45.9 Gy; $P = 0.0625$) and PET (median difference, 12.0 Gy; range, 11.2–12.7 Gy; $P = 0.0625$). The same trend was found for the SPECT–, PET–, and SPECT-MC–estimated mean absorbed doses in the phantom (Fig. 5). In both LAD and HAD ROIs, SPECT-MC–estimated mean absorbed doses were closest to the true dose.

The absorbed dose images and the dose–volume histograms for patient 5 are shown in Figure 6 to illustrate the differences that were found between the methods.

DISCUSSION

The objectives of this work were to introduce and validate a new ^{90}Y SPECT reconstruction algorithm incorporating a fast Monte Carlo simulator to model various image-degrading factors. The small differences observed between the UMCS-simulated projection images and the γ-camera measurements were probably due to assumptions made in the convolution-based forced-detection model. This model was originally developed for ^{99m}Tc simulation; in that scenario, almost all detected photons pass the collimator parallel to the septa. Mainly because of septal penetration, this supposition is less accurate for ^{90}Y, resulting in an underestimation of the final photon path length through the scatter object. This situation especially holds true for the photons detected in the tails of the line spread function in the line source experiment and explains the observed overestimation of the detection probability in this region. Other factors that may have limited the accuracy of the simulated projections include modeling of photon attenuation with a single $\mu_{central}$ value for each scatter map and the assumption of a circularly symmetric CDR, which ignores the star-shaped artifacts that are typical for septal penetration (*25*). Nevertheless, in general, the good agreement found between the simulated and the measured projection images indicates that the impact of these effects was probably small and that the image-degrading effects were sufficiently accurately modeled.

Consequently, the image contrast of ^{90}Y SPECT-MC observed in the IQ phantom experiment was significantly higher than that of state-of-the-art clinical SPECT, and the residual count error was reduced by 58%. The contrast-to-noise ratio for all spheres was higher for SPECT-MC, even though the image noise was about 3 times lower for clinical SPECT. Image noise and the residual count error in the lung insert were lower with SPECT-MC than with PET, indicating good performance of the compensation models with SPECT-MC. Although PET had higher image contrast in the smaller spheres, probably because of the higher resolution, SPECT-MC had higher contrast in the 2 largest spheres.

The SPECT and PET reconstruction parameters for optimal contrast recovery, which is more important for accurate quantification of local ^{90}Y content than reduction of noise, were determined in a previous study by our group (*7*). Accordingly, the number of iterations was varied between 1 and 120 in combination with various postreconstruction filters (0-, 5-, and 10-mm full width at half maximum) to find the SPECT-MC reconstruction protocol for optimal contrast recovery. A different set of reconstruction parameters may lead to optimized images for diagnostic purposes. Surprisingly, the contrast recovery coefficients for

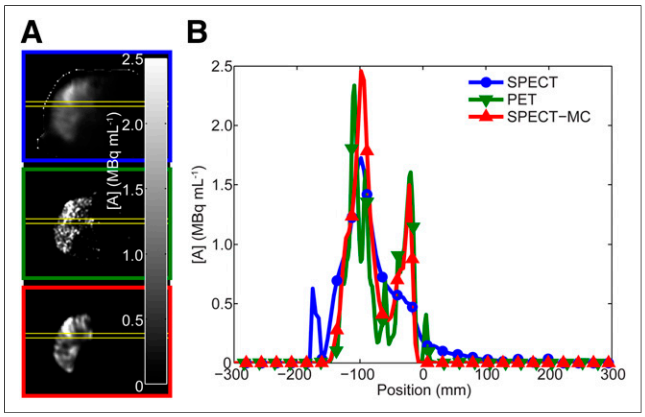

FIGURE 4. (A) Transverse slices through SPECT (blue), PET (green), and SPECT-MC (red) activity concentration images for patient 2. Images were linearly window leveled from 0 to 2.5 MBq mL^{-1}. (B) Activity concentration ([A]) distributions over profiles (averaged over bins between yellow lines).

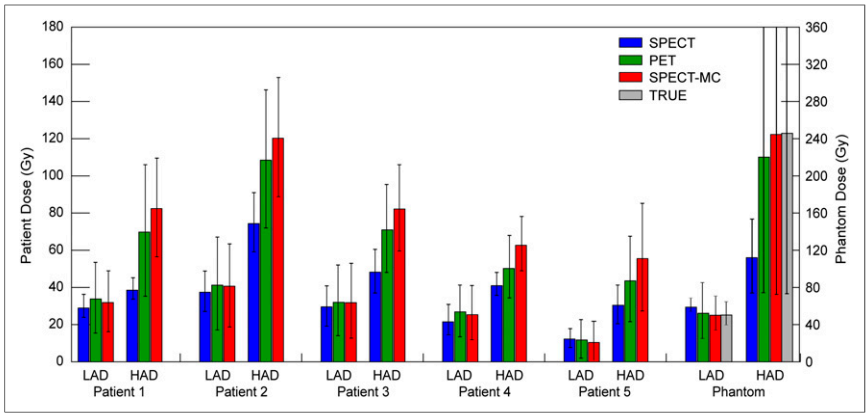

FIGURE 5. Bar plots of SPECT (blue), PET (green), and SPECT-MC (red) estimated mean absorbed doses in LAD and HAD ROIs for each patient and for phantom. True mean absorbed doses in LAD and HAD ROIs of phantom are illustrated by gray bars. Standard deviations of mean voxel values are depicted by error bars.

SPECT-MC (and SPECT) did not monotonically increase with increasing sphere diameter. The contrast recovery coefficient for the 13-mm sphere was 12% lower than that for the 10-mm sphere, and the contrast recovery coefficient for the 37-mm sphere was 2% lower than that for the 28-mm sphere. The difference between the 2 smallest spheres may have been a result of sampling errors because the SPECT voxel size is relatively large in comparison with the small sphere diameters. Additionally, these small ROIs may have been substantially influenced by image noise. For the 2 largest spheres, image contrast had converged to its final value after 60 iterations. The relatively small difference that was found was within measurement error, which was expected to be 2%–3% for the 2 largest spheres, on the basis of background noise.

The endpoint of the present study was to compare the absorbed doses estimated by SPECT, PET, and SPECT-MC. A possible limitation with regard to the creation of absorbed dose images is the assumption of deposition of the complete administered activity in the liver ROIs with 1-cm margins. Although we validated that no activity was deposited in organs other than the liver in the SPECT and PET fields of view, microspheres may (theoretically) have been deposited in organs outside the fields of view, such as in the top of the lungs. A second possible limitation concerns the use of the dose–point kernel to convert activity images to absorbed dose images. Although this approach is commonly used (*24*), it introduces extra blurring of already low-resolution images. A dose factor may be a better solution, especially for SPECT and SPECT-MC images. Despite these limitations, both PET– and SPECT-MC–estimated mean absorbed doses were shown to be in good agreement with the true absorbed dose in the LAD and HAD ROIs of the phantom. In the clinical study, the highest estimated mean absorbed doses in the HAD ROIs were found with SPECT-MC, followed by PET and SPECT. In the LAD ROIs, slightly higher estimated mean absorbed doses were found with PET than with SPECT-MC. These results reflect the trend that was found for radiation absorbed doses (and contrast recovery coefficients for larger ROIs) in the phantom study.

Although the HAD ROIs did not necessarily coincide with tumorous tissue, dosimetry results generally can be extrapolated to (larger) tumors because, with radioembolization, higher activity concentrations are expected in tumorous tissue than in the healthy liver parenchyma. Consequently, underestimation of the dose in well-perfused tumors (i.e., HAD regions) is expected with the clinical SPECT reconstruction algorithm, whereas the dose in poorly perfused tumors is likely to be overestimated. Clinical consequences may include patient selection for retreatment of "undertreated" tumors and erroneous conclusions from dose response analyses. SPECT-MC– and PET–based tumor dose estimates are more accurate, although differences between PET and SPECT-MC are to be expected for small and large tumors because of the different resolutions of the modalities. The clinical performance of both methods in terms of tumor response and survival prediction should be evaluated in a large clinical study.

The quantitative performance of SPECT-MC may be further improved by optimization of the detection window with Monte Carlo simulations, the use of photon energy weighting to determine (voxel-specific) μ-values instead of $\mu_{central}$, optimization of the number of scatter maps, or optimization of the number of simulated photons. The impact of these possible improvements on the quality of reconstructed images is a topic for further research. The total reconstruction time per subset (15 angles) on a single core of a 1.8-GHz Windows (Microsoft) desktop computer was 102 s (22 s for simulation of the scatter map, 48 s for application of the CDR, and 32 s for the backprojection step). In general, the reconstruction of posttreatment images is not as time critical as the reconstruction of diagnostic images. Nevertheless, the reconstruction time may be substantially reduced by saving certain information, such as rotated attenuation maps and CDR kernels, to the memory of a dedicated reconstruction computer instead of redundantly recalculating it in every iteration. Further improvements may be achieved by parallelization of the detection steps for the scatter maps, reduction in the number of simulated photons, or the use of a faster, simplified forward projection model in the first few iterations (*26*).

In a previous study, we showed that the IQ of state-of-the-art clinical PET was superior to that of bremsstrahlung SPECT (*7*). In the present study, we demonstrated that postradioembolization

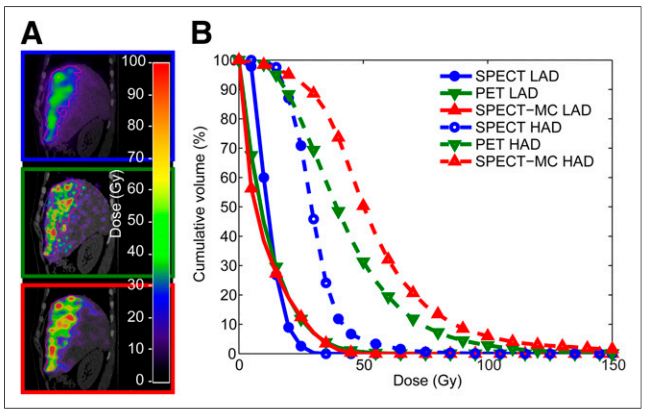

FIGURE 6. (A) Sagittal slices through SPECT (blue), PET (green), and SPECT-MC (red) estimated absorbed dose images fused with CT images for patient 5. HAD ROI boundary is illustrated by purple line. (B) Dose–volume histograms of LAD and HAD ROIs.

images obtained with a standard SPECT/CT scanner can be of sufficiently high quantitative accuracy for dosimetry purposes if reconstruction is done with adequate compensation models, especially for tumors with diameters larger than approximately 25 mm. The proposed method may be a cost-effective alternative to ^{90}Y PET because a pretreatment ^{99m}Tc-macroaggregated albumin SPECT scan is already part of the radioembolization procedure; therefore, no additional hardware investments are required.

CONCLUSION

We developed a new method for ^{90}Y SPECT reconstruction that includes Monte Carlo–based compensation for scatter and attenuation effects and energy-dependent modeling of the CDR. In a phantom experiment, the proposed reconstruction method improved the quantitative accuracy of the bremsstrahlung SPECT images relative to state-of-the-art clinical reconstruction. Evaluation of the estimated absorbed dose distribution in a small group of patients indicated that the proposed SPECT method may be used as an alternative to ^{90}Y PET.

DISCLOSURE

The costs of publication of this article were defrayed in part by the payment of page charges. Therefore, and solely to indicate this fact, this article is hereby marked "advertisement" in accordance with 18 USC section 1734. No potential conflict of interest relevant to this article was reported.

REFERENCES

1. Vente MA, Wondergem M, van der Tweel I, et al. Yttrium-90 microsphere radioembolization for the treatment of liver malignancies: a structured meta-analysis. *Eur Radiol.* 2009;19:951–959.
2. Kennedy AS, Salem R. Radioembolization (yttrium-90 microspheres) for primary and metastatic hepatic malignancies. *Cancer J.* 2010;16:163–175.
3. D'Arienzo M, Chiaramida P, Chiacchiararelli L, et al. Y-90 PET-based dosimetry after selective internal radiotherapy treatments. *Nucl Med Commun.* 2012;33:633–640.
4. Walrand S, Lhommel R, Goffette P, Van den Eynde M, Pauwels S, Jamar F. Hemoglobin level significantly impacts the tumor cell survival fraction in humans after internal radiotherapy. *EJNMMI Res.* 2012;2:20.
5. Chang TT, Bourgeois AC, Balius AM, Pasciak AS. Treatment modification of yttrium-90 radioembolization based on quantitative positron emission tomography/CT imaging. *J Vasc Interv Radiol.* 2013;24:333–337.
6. Lhommel R, van Elmbt L, Goffette P, et al. Feasibility of ^{90}Y TOF PET-based dosimetry in liver metastasis therapy using SIR-Spheres. *Eur J Nucl Med Mol Imaging.* 2010;37:1654–1662.
7. Elschot M, Vermolen BJ, Lam MGEH, de Keizer B, van den Bosch MAAJ, de Jong HWAM. Quantitative comparison of PET and bremsstrahlung SPECT for imaging the in vivo yttrium-90 microsphere distribution after liver radioembolization. *PLoS ONE.* 2013;8:e55742.
8. Willowson K, Forwood N, Jakoby BW, Smith AM, Bailey DL. Quantitative Y-90 image reconstruction in PET. *Med Phys.* 2012;39:7153–7159.
9. van Elmbt L, Walrand S, Lhommel R, Jamar F, Pauwels S. Quantitative comparison between LYSO and BGO PET-tomographs in ^{90}Y imaging [abstract]. *Eur J Nucl Med Mol Imaging.* 2010;37(suppl):S293.
10. Elschot M, Nijsen JFW, Dam AJ, de Jong HWAM. Quantitative evaluation of scintillation camera imaging characteristics of isotopes used in liver radioembolization. *PLoS ONE.* 2011;6:e26174.
11. Rong X, Du Y, Ljungberg M, Rault E, Vandenberghe S, Frey EC. Development and evaluation of an improved quantitative Y-90 bremsstrahlung SPECT method. *Med Phys.* 2012;39:2346–2358.
12. Hutton BF, Buvat I, Beekman FJ. Review and current status of SPECT scatter correction. *Phys Med Biol.* 2011;56:R85–R112.
13. Beekman FJ, de Jong HW, van Geloven S. Efficient fully 3-D iterative SPECT reconstruction with Monte Carlo-based scatter compensation. *IEEE Trans Med Imaging.* 2002;21:867–877.
14. De Jong HWAM, Slijpen ETP, Beekman FJ. Acceleration of Monte Carlo SPECT simulation using convolution-based forced detection. *IEEE Trans Nucl Sci.* 2001;48:58–64.
15. Xiao J, de Wit TC, Staelens SG, Beekman FJ. Evaluation of 3D Monte Carlo–based scatter correction for ^{99m}Tc cardiac perfusion SPECT. *J Nucl Med.* 2006;47:1662–1669.
16. Xiao J, de Wit TC, Zbijewski W, Staelens SG, Beekman FJ. Evaluation of 3D Monte Carlo–based scatter correction for ^{201}Tl cardiac perfusion SPECT. *J Nucl Med.* 2007;48:637–644.
17. Hendricks JS, McKinney GW, Waters LS, et al. *MCNPX Extensions, Version 2.5.0.* Los Alamos, CA: Los Alamos National Laboratory; 2005. Report LA-UR-05-2675.
18. Minarik D, Sjogreen GK, Ljungberg M. Evaluation of quantitative ^{90}Y SPECT based on experimental phantom studies. *Phys Med Biol.* 2008;53:5689–5703.
19. Rault E, Staelens S, Van Holen R, De Beenhouwer J, Vandenberghe S. Fast simulation of yttrium-90 bremsstrahlung photons with GATE. *Med Phys.* 2010;37:2943–2950.
20. de Jong HWAM, Wang WT, Frey EC, Viergever MA, Beekman FJ. Efficient simulation of SPECT down-scatter including photon interactions with crystal and lead. *Med Phys.* 2002;29:550–560.
21. Kamphuis C, Beekman FJ, van Rijk PP, Viergever MA. Dual matrix ordered subsets reconstruction for accelerated 3D scatter compensation in single-photon emission tomography. *Eur J Nucl Med.* 1998;25:8–18.
22. Zeng GL, Gullberg GT. Unmatched projector/backprojector pairs in an iterative reconstruction algorithm. *IEEE Trans Med Imaging.* 2000;19:548–555.
23. Kennedy A, Nag S, Salem R, et al. Recommendations for radioembolization of hepatic malignancies using yttrium-90 microsphere brachytherapy: a consensus panel report from the Radioembolization Brachytherapy Oncology Consortium. *Int J Radiat Oncol Biol Phys.* 2007;68:13–23.
24. Bolch WE, Bouchet LG, Robertson JS, et al. The dosimetry of nonuniform activity distributions: radionuclide S values at the voxel level. Medical Internal Radiation Dose Committee. MIRD Pamphlet No. 17. *J Nucl Med.* 1999;40(suppl):11S–36S.
25. Staelens S, de Wit T, Beekman F. Fast hybrid SPECT simulation including efficient septal penetration modelling (SP-PSF). *Phys Med Biol.* 2007;52:3027–3043.
26. de Wit TC, Xiao JB, Beekman FJ. Monte Carlo-based statistical SPECT reconstruction: influence of number of photon tracks. *IEEE Trans Nucl Sci.* 2005;52:1365–1369.